scientific reports

Check for updates

OPEN

Inverse designed aperiodic multilayer perfect absorbers for mid infrared enable tunability switchability and angular robustness

Masoumeh Nazari, Yaser M. Banad & Sarah Sharif✉

We present a class of inverse-designed, aperiodic multilayer graphene-based perfect absorbers operating in the mid-infrared spectrum (3–5 μm), a range vital for atmospheric transparency and advanced sensing. Our design leverages a fixed material sequence—graphene, PPSU dielectric spacers, and PbSe layers on a gold substrate—while achieving precise spectral tunability solely through layer thickness variation, enabling absorption peak control in 0.25 μm steps without any change in material composition. This physical tunability allows scalable fabrication of wavelength-specific devices using a single manufacturing process. We further demonstrate electrical switchability by dynamically modulating graphene's chemical potential (μc from 0 eV to 1 eV), enabling absorption amplitude control and wavelength redshifting without structural alteration. The proposed absorber achieves > 99.9% efficiency using only five graphene layers in a compact ~ 2 μm stack, offering significant advantages in size, weight, power, and cost. Our hybrid micro-genetic inverse design algorithm enables this performance while preserving > 90% absorption at incidence angles up to 52°, supporting broad angular robustness. Extensive simulation and field distribution analyses confirm the role of plasmonic confinement and impedance matching. Additionally, we validate the design's fabrication tolerance and benchmark its performance against recent state-of-the-art absorbers. By combining advanced inverse design with nanophotonic structures, our work advances the field of mid-infrared absorbers, providing a scalable and efficient platform for next-generation optical devices.

In recent years, the ability to precisely control optical absorption has garnered significant attention due to its critical role in applications such as environmental monitoring[1], thermal emitting[2], sensing[3–5], photodetection[6–8], and solar energy harvesting[9]. Perfect absorbers (PA)s, engineered to achieve near-unity absorption, have proven indispensable across electromagnetic frequencies, including microwave[10], terahertz[11,12], infrared[13–15], and visible wavelengths[16]. Among these, the mid-infrared (mid-IR) spectrum (3–5 μm) is of particular importance due to its minimal atmospheric absorption, enabling critical applications in spectroscopy[17] and sensing applications[18]. Despite recent progress, mid-IR absorbers often remain static in their optical response and exhibit limited angular performance, suggesting a need for designs that can offer dynamic tunability and switchability. To address this, various advanced architectures have been proposed, including metasurface, multilayer, and metamaterial-based absorbers. For instance, Fang et al.[19] introduce a mid-IR wideband perfect absorber, composed of multiple layers including Al_2O_3 and silicon (Si) with embedded titanium (Ti) ring, achieving exceptional absorption performance across the entire spectrum. Bossard et al.[20] demonstrated metamaterial absorbers with broad bandwidth through a genetic algorithm-optimized metallic screen. However, despite their high absorption efficiency, the structures lack tunability, limiting their adaptability to dynamic infrared applications. Additionally, the fabrication process is complex due to the precise embedding of the Ti ring within the Si layer, posing challenges for large-scale manufacturing. Corrigan et al.[21] proposed a broadband mid-IR absorber based on a periodic multilayer structure of dielectric and thin metal films, achieving near-perfect absorption across a wide spectral range. Their design optimizes absorption by adjusting the number of layers, incorporating an anti-reflective coating, and utilizing a reflective metallic bottom layer. However, the structure is extremely thick, requiring up to 21 layers, with each dielectric layer being 1.34 μm thick. Sahu and Behera[22]

The School of Electrical and Computer Engineering, University of Oklahoma, Norman, OK 73019, USA. ✉email: s.sh@ou.edu

proposed a mid-infrared broadband absorber based on a multilayer structure of aluminum-doped zinc oxide (AZO) and dielectric films. Their design achieves over 95% absorption in the 7.5–20 μm range, utilizing optical interference and constructive resonance. Their proposed structure could not provide perfect absorption, and the absorber layer relies on adjustments to the doping concentration. Its design consists of ten layers (five pairs of AZO and dielectric films), resulting in a total thickness of 8 μm, with each dielectric layer measuring 1.5 μm. This considerable thickness limits integration into compact devices.

Further advancing the field, semiconductor-based absorbers, such as paper presented by Wang et al.[11], achieve near-perfect absorption but remain limited to static spectral responses. On the other hand, narrowband designs, like Chen et al.[23], integrate dielectric metasurfaces for precise band compression but sacrifice flexibility in adjusting resonance peaks[24,25]. Although these designs exhibit impressive performance, they often lack dynamic tunability or rely on traditional approaches that require a complete structural redesign—including material sequence and layer geometry—for each target wavelength, necessitating new fabrication setups for every configuration[11,26–29].

Graphene-based absorbers have emerged as a promising alternative, offering dynamic tunability through the manipulation of chemical potential. Yao et al.[30] demonstrated an electrically tunable metasurface perfect absorber using optical antennas on graphene integrated into a subwavelength optical cavity. Their design enables high-speed optical modulation with a modulation depth of up to 100% in the mid-IR range (5–7 μm). However, despite its thin profile, the fabrication process poses significant challenges due to the need for precise nanopatterning of the metasurface and accurate control of the cavity dimensions, which can impact the device's performance and scalability. Safaei et al.[31] developed a wide-angle, dynamically tunable infrared absorber based on large-area nanopatterned graphene. Their design utilizes hexagonal arrays of nanoholes and nanodisks to excite Dirac plasmons, enhancing light-matter interactions. The nanodisk array achieves a peak absorption of up to 90%, while the nanohole array reaches around 60% in the mid-IR range (8–12 μm). Absorption can be electrostatically tuned by modulating the graphene's Fermi level. However, the lack of high-precision absorption and the complexity of the fabrication process remain the main challenges. Sun et al.[32] proposed a tunable, nearly perfect absorber based on graphene metamaterials, utilizing a periodic array of graphene ribbons and inverse slots in a thin graphene film to achieve near-total absorption in the mid-IR range. The structure enables strong plasmonically induced absorption and metamaterial resonance, resulting in an absorbance of up to 97.12%. Additionally, the absorption spectrum can be dynamically tuned by modifying the chemical potential of graphene. Despite its thin profile, there is still room to achieve perfect absorption, and nanofabrication techniques to pattern the graphene metamaterial and maintain accurate alignment of the bright and dark modes are still challenging. Some researchers also have incorporated phase-change materials (e.g., vanadium dioxide and germanium antimony telluride) into PA designs, enabling tunable photonic devices[33–39]. However, these materials often require high-power inputs, limiting their effectiveness in low-power systems.

In comparison to recent mid-infrared absorbers, including both multilayer and tunable graphene-based designs, our proposed aperiodic multilayer graphene absorber offers a significantly thinner profile than most multilayer structures while providing tunability and switchability due to the unique properties of graphene, material order of the structure and optimization method. Additionally, compared to metasurface and metamaterial absorbers, it requires a less complex fabrication process, making it more practical for large-scale implementation. In our prior work[2,40–43], we explored graphene-based aperiodic multilayer structures using 8–32 graphene layers to achieve tunable thermal emission at a single wavelength (3.34 μm). However, these designs were constrained by excessive layer counts, limited spectral coverage, and reduced angular robustness—challenges that hinder scalability for real-world infrared systems.

In this work, we introduce a highly versatile, fabrication-friendly, perfect aperiodic absorber architecture that addresses several persistent challenges in mid-IR absorber design. The term 'aperiodic multilayer' in this work refers to a structure composed of a fixed material sequence (graphene and dielectric) with non-repeating, optimized layer thicknesses along the z-direction. Unlike classical periodic stacks such as Bragg reflectors[44,45], which rely on uniform periodicity for spectral response, our design leverages deterministically aperiodic thickness modulation to achieve precise spectral tunability, switchability, and angular robustness without changing material composition. Its resonance wavelength can be precisely tuned across the full 3–5 μm range by modifying only the layer thicknesses, a form of dynamic tunability that eliminates the need for lithographic patterning or redesign. This modular design enables a single fabrication process to generate multiple high-performance absorbers across the spectrum, dramatically simplifying manufacturing and enabling scalable production. The structure achieves ultra-high absorption efficiency (> 99.9%) with only five graphene layers, resulting in a total thickness of ~ 2 μm, and supporting exceptional SWaP-C performance. In addition to physical tunability, it also offers electrical switchability, allowing dynamic modulation of absorption intensity at each wavelength via electrostatic control of graphene's chemical potential. The inverse design algorithm has been developed to demonstrate angular robustness, maintaining > 90% absorption at incident angles up to 52°. Together, these features establish a compact, reconfigurable, and energy-efficient platform for a broad range of mid-IR applications, including environmental sensing, thermal imaging, and stealth technology.

Section II of our paper delves into the meticulous selection process of materials integral to the construction of our advanced PAs, accompanied by a detailed explanation of our computational and optimization methodologies. Section III showcases the results obtained from our optimized structure, highlighting its remarkable tunability and switchability characteristics, as well as examining the absorber's performance across various incident angles in both TE and TM polarizations, ensuring its applicability in real-world scenarios. In the concluding section, we summarize the key findings, compare the results with existing structures, and discuss their future implications.

Design and characteristics analysis of graphene-based perfect absorber

Utilizing deep knowledge of materials, developing an advanced inverse design hybrid approach, and using computational electromagnetics to solve Maxwell's equations, our structure is an aperiodic multilayer structure consisting of alternating layers of graphene and a polymer dielectric, sandwiched between two Lead Selenide (PbSe) layers and supported by a semi-infinite gold (Au) substrate as shown in Fig. 1.

A. Material selection and structural design

Graphene serves as the core material, offering exceptional tunability and optical properties due to its high electron mobility, optical transparency, and conductivity. Its ability to support surface plasmons in the mid-IR and terahertz ranges makes it highly effective for applications such as photodetection, modulation, and absorption[41,46–52]. The optical conductivity of graphene, governed by the Kubo formula[41,53], is a critical parameter for understanding its absorption behavior and can be expressed as:

$$\sigma\ (\omega\ ,\mu_{\ c},\Gamma\ ,T)=-\frac{ie^{2}\ (\omega\ +i2\Gamma\ )}{\pi\ \hbar^{2}}\left[\frac{1}{(\omega\ +i2\Gamma\ )^{2}}\int_{0}^{\infty}\left(\frac{\partial\ n_{f}\ (\epsilon)}{\partial\ \epsilon}-\frac{\partial\ n_{f}\ (-\epsilon)}{\partial\ \epsilon}\right)\epsilon d\epsilon-\int_{0}^{\infty}\frac{n_{f}\ (-\epsilon)-n_{f}\ (\epsilon)}{(\omega\ +i2\Gamma\ )^{2}-4\left(\frac{\epsilon}{\hbar}\right)^{2}}d\epsilon\right] \quad (1)$$

where $n_{f}(\epsilon)=1/\{1+\exp[(\epsilon-\mu_{c})/(k_{B}T)]\}$ is Fermi-Dirac distribution, ω is radian frequency, e is the electron charge, $\hbar$ is reduced Plank constant, T is the temperature, μ_{c} is the CP, k_{B} is the Boltzmann constant, $\Gamma=e\,v_{F}^{2}/2\mu_{c}$ is the charge particle scattering, and $V_{F}=10^{6}m/sis$ the Fermi velocity. These scattering rates are consistent with multilayer graphene structures, as supported by experimental findings[54]. Graphene's optical conductivity comprises intraband and interband contributions, representing absorption by free carriers and valence-to-conduction band transitions, respectively. In the mid-IR range, intraband transitions contribute significantly, becoming comparable to interband transitions. This interplay enables control over the refractive index by tuning the chemical potential in graphene[55]. Consequently, the propagation of electromagnetic waves in graphene can be actively managed through chemical doping, external electric or magnetic fields, or optical excitation, which electrically modulates its optical absorption properties[2,51]. Thus, applying a DC bias electric field perpendicular to the graphene/dielectric interface adjusts the charge carrier density, thereby controlling the refractive index within the graphene layers[51,55]. Optical conductivity, a complex quantity describing the surface current induced by light in graphene, remains a cornerstone for explaining its optical behavior. Crucially, this parameter depends on the chemical potential (Fermi energy)[56,57]. By fine-tuning the chemical potential, one can dynamically alter graphene's optical characteristics, enabling its application in highly tunable photonic and optoelectronic devices.

While graphene absorbs efficiently due to its thickness, relying solely on the overall absorption of the entire structure limit the tunability and switchability performance of the structure. So, incorporating multiple graphene layers can significantly enhance absorption in the mid-IR range. Introducing Polyphenylsulfone (PPSU) as a dielectric spacer between graphene layers allows for precise control over interlayer spacing, further optimizing absorption characteristics. PPSU's excellent thermal stability and dielectric properties make it an ideal candidate for this purpose[58–64].

The combination of graphene's tunable absorption with PPSU spacers plays an important role in control over absorption pick, and tunability of the structure. PbSe serves as a medium capable of absorbing mid-IR light, and its deposition can be easily achieved through thermal evaporation methods[65], enabling seamless integration into the multilayer configuration. PbSe, a narrow bandgap semiconductor with a direct bandgap of approximately 0.27 eV at room temperature, is highly responsive to mid-IR wavelengths, particularly in the 3–5 μm range, and serves as an effective medium for absorbing mid-IR light[66–68]. By strategically placing PbSe layers at the top and

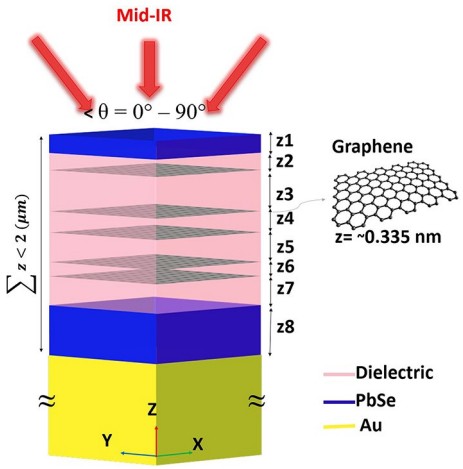

Fig. 1. The schematic of the proposed Perfect Absorber composed of alternating layers of graphene and dielectric, which are sandwiched between two PbSe layers with a total thickness of around 2 μm. A semi-infinite gold layer is used as the substrate.

bottom, several key benefits are realized. PbSe's strong absorption in the mid-IR range complements graphene's tunable absorption, significantly enhancing overall absorption efficiency. Furthermore, the integration of PbSe with graphene improves photodetection capabilities by combining graphene's high mobility with PbSe's robust light absorption, resulting in superior photodetector performance. Additionally, PbSe's excellent thermal stability ensures the device maintains optimal performance under varying temperature conditions. Thus, the inclusion of PbSe layers not only boosts mid-IR light absorption but also improves the overall efficiency, thermal stability, and functionality of the graphene-PPSU multilayer structure, making it highly suitable for advanced applications in mid-IR photodetection and sensing.

The strategic ordering of materials in our structure plays a fundamental role in achieving perfect absorption across the 3–5 μm range through thickness modulation alone. The top PbSe layer serves as an initial broadband absorber, while the subsequent graphene-PPSU alternating layers create a precisely engineered electromagnetic environment. This arrangement enables surface plasmon excitation at the graphene-dielectric interfaces[69], with the PPSU spacers controlling the coupling strength between adjacent graphene layers. When incident light encounters this structure, it undergoes multiple interactions: initial absorption by PbSe, plasmonic interactions within the graphene-PPSU stack, and finally, reflection from the gold substrate for a second pass through the structure. The thickness of each individual layer in our multilayer structure is meticulously designed to critically influence the overall absorption performance and spectral characteristics. The PbSe layers, graphene sheets, and PPSU spacers are all precisely tuned, leveraging the principles of thin-film interference and impedance matching. The thicknesses of the PbSe layers are selected to maximize their inherent absorption capabilities within the mid-IR range, acting as efficient initial absorbers and contributing to a broad absorption profile. Furthermore, the thickness of the dielectric PPSU spacers between graphene layers is paramount in controlling the plasmonic interactions and resonant behavior. These spacers, acting as a resonant cavity, directly influence the coupling strength between adjacent graphene layers and dictate the wavelengths at which constructive interference and thus, enhanced absorption, occurs. The precise interplay between the layer thicknesses, combined with the material properties, allows us to effectively control the impedance of the structure at the target wavelengths, minimizing reflection and maximizing the absorption of incident electromagnetic radiation. This fine-tuning of layer thicknesses, crucial for achieving the desired performance, was achieved through an inverse design approach, employing a micro-genetic algorithm, detailed in Section B. This powerful optimization technique allowed us to iteratively determine the optimal thicknesses for each layer, guided by our objective of maximizing absorption across the 3–5 μm mid-IR range.

The gold substrate's reflection ensures maximum light-matter interaction within the structure, effectively eliminating transmission and enhancing absorption through constructive interference of the reflected waves with the incident light[25,70].

B. Optimization methods

Our research employs an inverse design approach to optimize the multilayer structure by starting with the desired optical performance and working backward to identify the necessary structural parameters. This methodology is particularly effective for complex multilayer systems, where achieving optimal configurations through intuitive design is often impractical. As illustrated in Fig. 2(a), this approach contrasts with traditional forward modeling by using performance targets to drive the design process. In the forward model, we solve Maxwell's equations using the Transfer-Matrix Method (TMM) and Finite-Difference Time-Domain (FDTD)[2,71] techniques to evaluate the optical response of candidate structures. These computational methods enable accurate simulations of multilayer optical properties, allowing for a rigorous assessment of absorption efficiency and spectral characteristics.

To implement this strategy, we adopted a hybrid optimization technique[72]that combines a micro-genetic algorithm (micro-GA) for global exploration with a local optimization algorithm for fine-tuning. The micro-GA is an iterative optimization procedure that begins with a randomly initialized population of potential solutions, evolving them through genetic operations such as selection, crossover, and mutation[73]. This evolution improves solutions over successive generations, with frequent restarts to prevent the algorithm from becoming trapped in local optima. Once the population converges, the local optimization algorithm refines the best solution by exploring the surrounding parameter space to locate the nearest local optimum. The best structure found during this process is retained, and the cycle is repeated iteratively until convergence criteria are satisfied, as shown in Fig. 2(b). This hybrid approach is particularly powerful for designing aperiodic multilayer structures because it combines the broad exploration capabilities of the micro-GA with the precision of local optimization. The micro-GA, which uses a smaller population size than conventional genetic algorithms, offers significant advantages, including reduced computational overhead, faster convergence, and improved resilience against premature stagnation due to its frequent restarts and diversity-preserving mechanisms. Meanwhile, the local optimization stage ensures fine-tuning of layer thicknesses, enabling the design to meet strict performance criteria. Together, these methods enable the efficient and precise optimization of multilayer structures, allowing for the dynamic modulation of absorption peaks across the 3–5 μm range by adjusting layer thickness alone. This hybrid optimization achieves high resolution, with absorption peaks shifted in 0.25 μm increments, while maintaining the compactness of the structure with an overall thickness of less than 2 μm. The ability to achieve such fine control without altering the material composition ensures that the structure meets SWaP-C requirements, making it ideal for mid-IR sensing applications[72,74,75].

Table 1 presents a summary of the parameters and methods used in the study. Additionally, Supplementary S1 provides further details about simulation parameters and computational methodology.

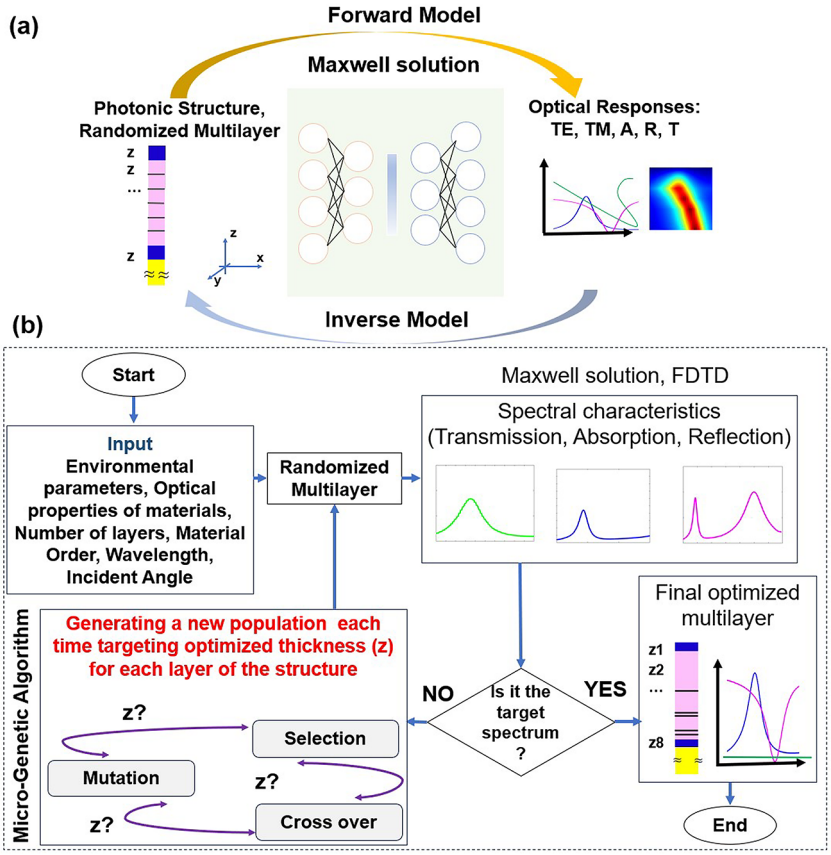

Fig. 2. The optical response of randomized multilayers is obtained using a forward model, followed by the utilization of an inverse model to generate the optimized multilayers; (b) The optimization approach, integrating the Genetic Optimization Algorithm (GOA) and a local optimization algorithm, strategically refines aperiodic multilayer structures for optimal absorptance. The continuous cycle of stochastic initialization, population evolution, is visually elucidated, highlighting the commitment to maximizing absorptance through the lens of inverse design.

Parameter	Characterization
Wavelength range	3–5 (μm)
# of layer	11
Graphene model	Kubo formula
Chemical Potential (μc)	0 – 1.0 (eV)
Layer thickness	~10–500 (nm)
Optimization method	Inverse Design /Micro-genetic algorithm
Simulation methods	TMM, FDTD
Boundary conditions	Periodic (x/y), PML (z)
Mesh resolution	Extremely Fine
Incident angle range	0–90 degree
Temperature	300 (K)
Environment	Air

Table 1. Summary of detail of parameters and methods used in the study.

Result and discussion

A. Spectral tunability via thickness variation

The proposed aperiodic multilayer structures exhibit remarkable spectral tunability across the mid-IR range, particularly within the 3–5 μm, which is critical for thermal imaging, gas sensing, and other applications requiring minimal atmospheric absorption. By adjusting the individual layer thicknesses while keeping the material sequence fixed, each structure can be precisely engineered to achieve near-unity absorption at a target

wavelength. This form of physical tunability enables systematic control over the absorption peak location without requiring structural redesign or changes in material composition, as shown in Fig. 3.

To demonstrate this capability, nine optimized structures, labeled (a) through (i), were designed to resonate at evenly spaced wavelengths between 3 μm and 5 μm in 0.25 μm intervals: 3 μm, 3.25 μm, 3.5 μm, 3.75 μm, 4 μm, 4.25 μm, 4.5 μm, 4.75 μm, and 5 μm, respectively. As shown in Fig. 3(a), all structures achieve nearly perfect absorption at their designated wavelengths. The gray-highlighted background region in the figure represents the 3–5 μm mid-IR atmospheric transmission window, illustrating how each design successfully aligns with this low-loss spectral range. Despite differences in their optimized thickness profiles, all structures share a consistent material stacking order and maintain a total thickness of approximately 2 μm. Figure 3(b) presents the unique layer thickness distributions for each structure, highlighting that precise spectral tuning is achieved solely through geometrical modifications. This design process, powered by an inverse design framework with a micro-genetic algorithm, eliminates the need for structural redesign or lithographic reconfiguration, enabling scalable fabrication of multi-wavelength absorber arrays from a single standardized material platform.

The detailed layer thicknesses of the optimized structure have been provided in Supplementary Material S2. Table S1, in supplemental materials, is the raw data obtained directly from the inverse design optimization algorithm. These values represent high-precision numerical outputs and include decimal-level thicknesses that are not directly achievable in practice. For simulation and fabrication considerations, the thickness values were subsequently rounded to the nearest practical values, as presented in Table S2, which also includes the tolerance margins applied to the thinnest layers. The impact of these tolerances on absorption performance is analyzed in detail in Section III.D: Field Distribution and Structural Robustness.

In addition, to further highlight the effectiveness of our optimization algorithm in designing high-performance absorbers and to elucidate the critical role of layer thickness in shaping absorption characteristics, we perform a detailed comparative analysis between optimized and non-optimized multilayer structures, as shown in Fig. 4.

Structure 1, optimized using inverse design, achieves a sharp and precise absorption peak at 4 μm. In contrast, Structures 2, 3, and 4 use uniform, non-optimized layer thicknesses derived from the optimized design: the maximum thickness (487.67 nm), minimum thickness (62.17 nm), and average thickness (274.92 nm) of

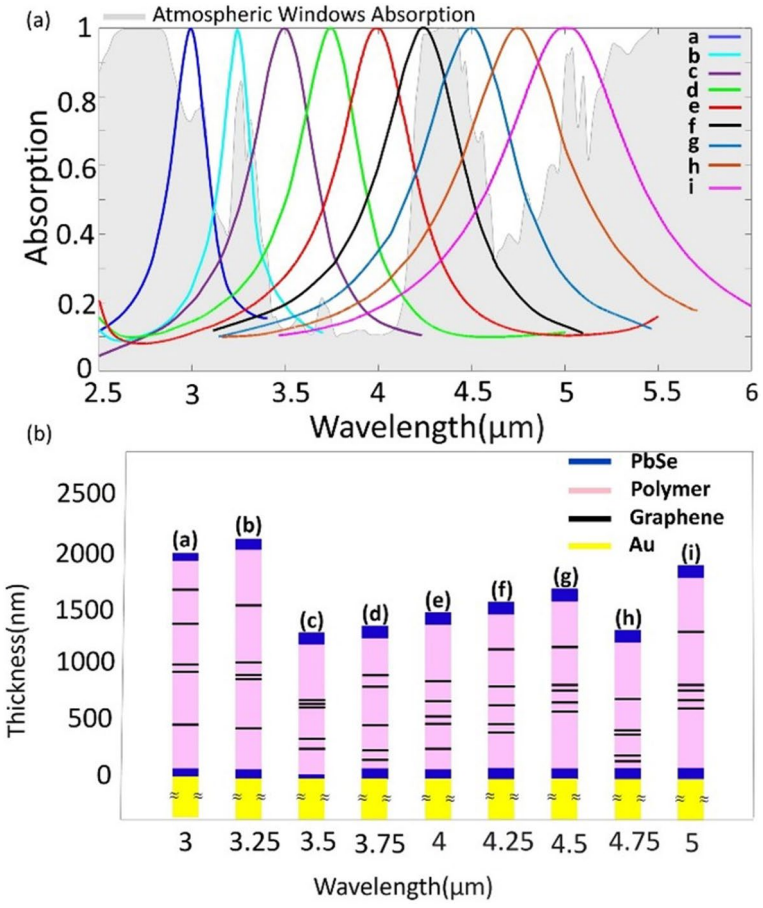

Fig. 3. (a) Absorption spectra of the proposed absorbers (Structures a, b, c, d, e, f, g, h, and i are optimized to achieve absorption peaks at 3 μm, 3.25 μm, 3.5 μm, 3.75 μm, 4 μm, 4.25 μm, 4.5 μm, 4.75 μm, and 5 μm, respectively). (b) Nine optimized aperiodic multilayer absorbers consist of alternating layers of dielectric and graphene each tailored to achieve specific absorption peaks corresponding to (a).

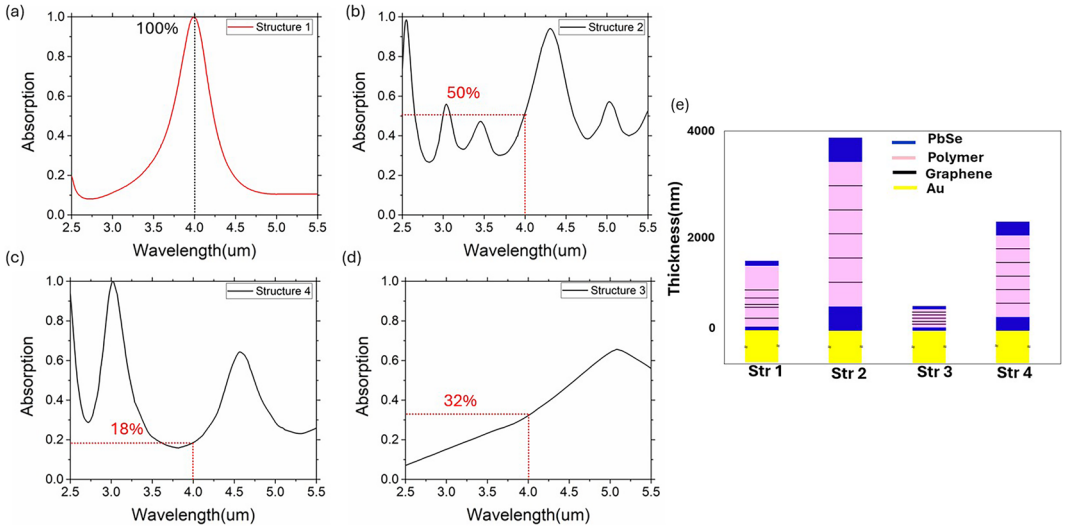

Fig. 4. Comparison of absorption performance between the optimized structure and non-optimized structures with uniform layer thicknesses. (a) The absorption spectrum of Structure 1, the optimized design generated using the inverse design framework, which achieves 100% absorption at 4 μm. (b–d) Absorption spectra of three non-optimized structures with equal thickness layers: Structure 2 uses the maximum thickness (487.67 nm), Structure 3 uses the minimum thickness (62.17 nm), and Structure 4 uses the average thickness (274.92 nm) derived from Structure 1. None of these configurations achieve perfect absorption—only 50%, 32%, and 18% are achieved at 4 μm in Structures 2, 3, and 4, respectively—highlighting the critical importance of precise thickness tuning. (e) Structural comparison showing the material layer distributions in each design. While the material sequence and composition are kept constant, only the optimized, aperiodic thickness profile in Structure 1 enables impedance matching and constructive interference, which are required for near-unity absorption. These results strongly validate the necessity of the inverse design optimization algorithm in engineering high-performance multilayer absorbers with tailored spectral responses.

Structure 1, respectively. These non-optimized designs exhibit significant deviations in absorption peak position and substantially lower absorption efficiency compared to the optimized structure. The absorption peaks for Structures 2, 3, and 4 are shifted away from 4 μm, with broader and less efficient profiles, emphasizing the critical importance of precise layer thickness control.

B. Electrical switchability via chemical potential modulation

In addition to physical tunability via thickness variation, the proposed structure exhibits electrical switchability through the modulation of the graphene chemical potential (μc). Figure 5 depicts the absorption spectra of nine optimized structures as a function of the μc. For structures (a) and (b), an elevation in the chemical potential from 0 eV to 1 eV results in a shift of the absorption peak from 3 μm to 3.05 μm and from 3.25 μm to 3.29 μm, respectively. In these cases, the graphene layers contribute approximately 20% to the total absorption, with PbSe dominating the absorption profile. In contrast, the structures optimized for longer wavelengths—shown in Fig. 5(c–h)—exhibit a more substantial change in absorption intensity and redshift under varying μc. This is particularly evident for designs targeting wavelengths of 3.5 μm and higher, where the absorption efficiency drops by up to 50%, as illustrated in Fig. 6(a). These changes can be attributed to the tunable optical conductivity of graphene, as described by the Kubo formula (Eq. 1). As μc increases, intraband transitions in graphene become more dominant, leading to a rise in carrier density. This, in turn, increases the plasma frequency, thereby altering the resonance conditions within the multilayer structure. Simultaneously, the effective refractive index of the graphene layers increases, while the imaginary part of the permittivity decreases, resulting in weaker plasmonic confinement and a corresponding reduction in absorption efficiency.

The absorption spectrum of the structure optimized at 4 μm is shown in Fig. 6(b), where increasing the chemical potential from 0 eV to 1 eV reduces the peak absorption from 100 to 56%. This amplitude modulation is directly tied to a redistribution of absorption among the constituent materials, as detailed in Fig. 6(c). There, the absorption contribution of each material is shown for both $\mu c = 0.0$ eV and $\mu c = 1.0$ eV. Notably, at $\mu c = 0.0$ eV, graphene layers contribute 48% to the total absorption, while PbSe absorbs the majority of the remainder. However, when μc increases to 1.0 eV, graphene's contribution drops sharply to just 2%, and 44% of the incident energy is no longer absorbed, highlighting the absorber's electrical switchability. This behavior stems from the fact that the energy absorbed in the multilayer structure is influenced by the effective refractive index, which itself depends on the chemical potential of graphene. The observed shift in absorption characteristics confirms the feasibility of creating electrically reconfigurable optical absorbers, in which both amplitude and material-selective absorption can be dynamically tuned.

The observed modulation in absorption amplitude and material contribution highlights the potential of this structure as a reconfigurable mid-IR absorber. The ability to dynamically control absorption via chemical

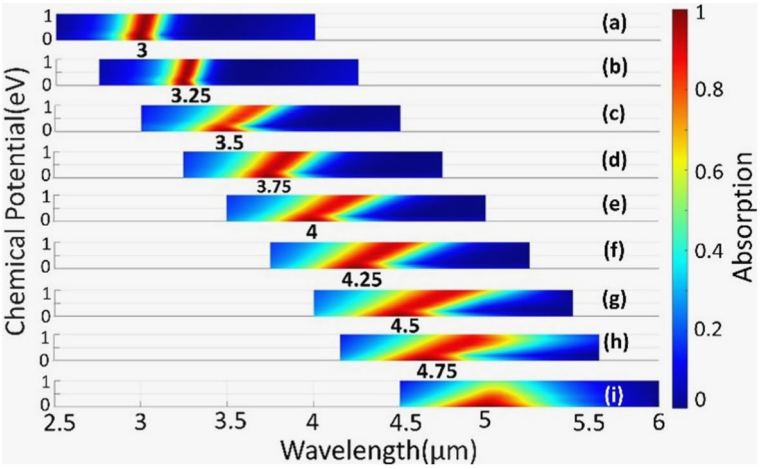

Fig. 5. The impact of varying chemical potential on the absorption characteristics of the proposed PAs, (a) and (b) A light redshift occurs with an increase in chemical potential, accompanied by achieving perfect absorption at these specific wavelengths; (c), (d), (e), (f), (g), (h) Tunable absorption through chemical potential modulation. Increasing the chemical potential leads to a redshift in absorption peaks towards longer wavelengths. (i) Switchable absorption through chemical potential modulation. The perfect absorptance of unity at 5 μm for a chemical potential of 0 can be switched to an absorptance of 0.55 by adjusting the chemical potential to 1 eV.

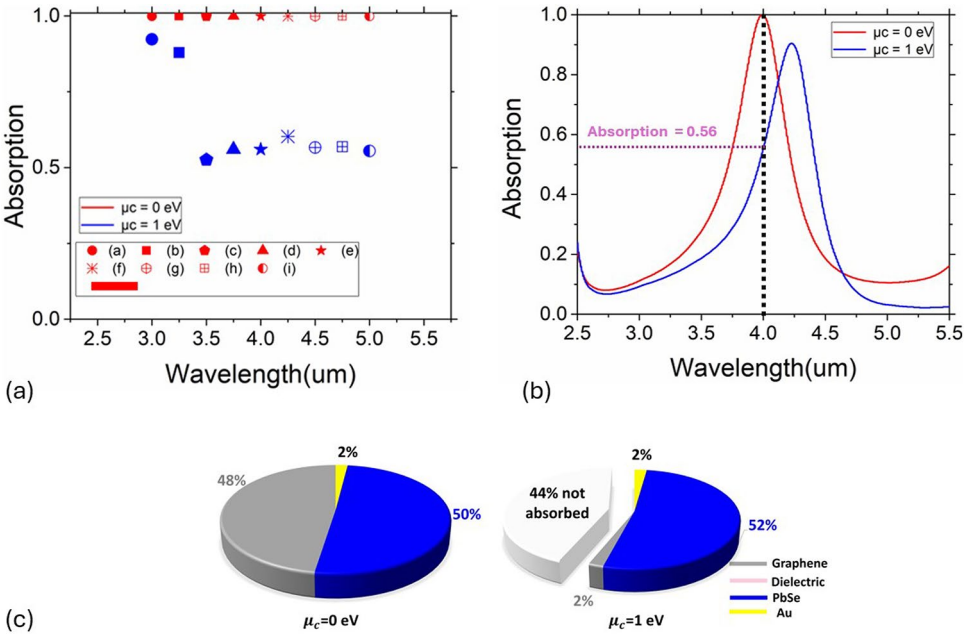

Fig. 6. (a) Electrical switchability of the absorber across all nine optimized structures (a–i) within the 3–5 μm range. Absorption is shown at two chemical potential states: μc = 0 eV (red) and μc = 1 eV (blue), revealing reduced absorption with increased μc while maintaining peak alignment. (b) Absorption spectrum of the structure optimized at 4 μm, showing a peak absorption drop from 100–56%. (c) Material-wise absorption contribution for the same 4 μm structure at μc = 0 eV and μc = 1 eV. At higher μc, absorption in graphene drops to 2%, and 44% of the incident energy remains unabsorbed, demonstrating strong electrical switchability.

potential—without modifying the physical structure—enables practical applications in adaptive filtering, tunable sensing, and programmable thermal emission systems.

C. Stability of absorption across incident angles

In our study, although we have effectively optimized our structures for perfect absorption under normal incident light, we recognize the significance of preserving high absorption efficiency when exposed to different incident angles for practical applications. In response to this concern, we have conducted a comprehensive examination

of how the incident angle impacts the performance of our proposed PAs. Figure 7 presents a comprehensive overview of absorption spectra at various incident angles, spanning from θ = 0° (normal incidence) to θ = 90° (grazing incidence), for all optimized multilayer structures designed to absorb within the 3 to 5 μm range, with 0.25 μm intervals. As the incident angle increases, the absorption spectra shifts to shorter wavelengths (blueshift), consistently observed across all optimized structures. This phenomenon arises from several interrelated physical mechanisms. First, the phase-matching conditions for constructive interference change with angle due to variations in the optical path length, which decreases as cos θ. This necessitates shorter wavelengths to maintain resonance conditions. Second, the dispersion relation of graphene surface plasmons, integral to the multilayer structure's absorption, is angle-dependent. An increase in the incident angle alters the momentum matching conditions, leading to resonances at higher energies (shorter wavelengths). Additionally, the effective optical thickness of each layer, defined as $d_{effective} = d_{actual} \times \cos\theta$, decreases with angle, further shifting resonances to shorter wavelengths. Lastly, angular incidence modifies the coupling strength between adjacent layers, subtly influencing the light-matter interaction and shifting the absorption peaks. These factors collectively explain the observed blueshifts while preserving high absorption efficiency up to relatively large angles. This detailed analysis supports the robustness of the proposed structures for practical applications requiring angular stability. Despite these shifts, the proposed absorbers demonstrate remarkable resilience in maintaining high absorption levels. The absorption rate exceeds 90%, even at incident angles as steep as approximately 46, 47, 49, 50, 52, 55, 57, 58, and 60 degrees for structures (a), (b), (c), (d), (e), (f), (g), (h), and (i) respectively.

These findings hold importance as they validate the robustness and applicability of our PA designs. The capacity to maintain nearly perfect absorption across a broad range of incident angles not only underscores the effectiveness of our structures but also underscores their suitability for practical applications, where light commonly approaches from diverse angles.

Figure 8 shows the inherent controllability and tunability of our design in different incident angles. We analyze the effect of varying chemical potential and incident angle on one of structure as an example, here the Fig. 4(e). The results highlight how changes in chemical potential and incident angle influence the absorptive capacity of this structure, optimized for peak absorption at 4 μm. This figure provides a clear visualization of the structure's dynamic adjustability, showing that altering the chemical potential from 0 eV to 1 eV shifts the absorption peak at λ = 4 μm towards higher wavelengths under normal incidence while varying the incident angles for constant chemical potentials causes the absorption peak to shift towards lower wavelengths. Nevertheless, it is evident that alterations of both chemical potential and incident angle lead to a decline in absorption performance. Despite this, the structure maintains a high absorption peak above 0.9 for angle adjustments up to 52 degrees. This demonstrates the proposed structure's capability to function as a near-PA in practical situations where light incidence angles can vary.

D. Field distribution and structural robustness

Figure 9 illustrates the absorption spectrum for both TE and TM polarizations, showcasing the impact of varying the incident angle for structure (e). It is evident that the absorption performance is superior for TM polarization compared to TE polarization. The structure can operate close to a PA with 90% absorption, allowing adjustments in the angle up to 60 degrees for TM polarization, while reaching a limit of 47 degrees for TE polarization. This difference underscores the structure's ability to handle a wider range of incident angles effectively when the magnetic component of the light is more engaged, providing greater flexibility in applications where the angle of incidence cannot be precisely controlled.

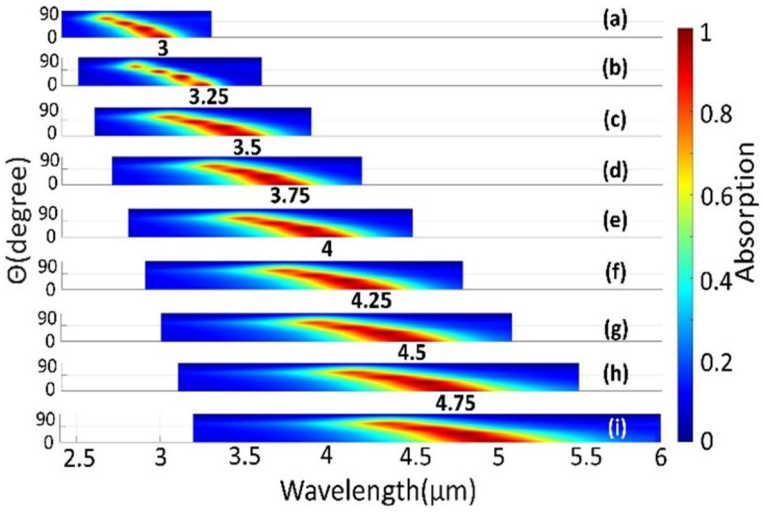

Fig. 7. The effect of incident angle on absorption of the proposed PAs. The observation reveals a blue shift in absorption peaks as incident angles increase across all structures. These proposed structures consistently sustain their PA status, achieving over 90% absorption, up to incidence angles of 46, 47, 49, 50, 52, 55, 57, 58, and 60 degrees for structures (a), (b), (c), (d), (e), (f), (g), (h), and (i), respectively.

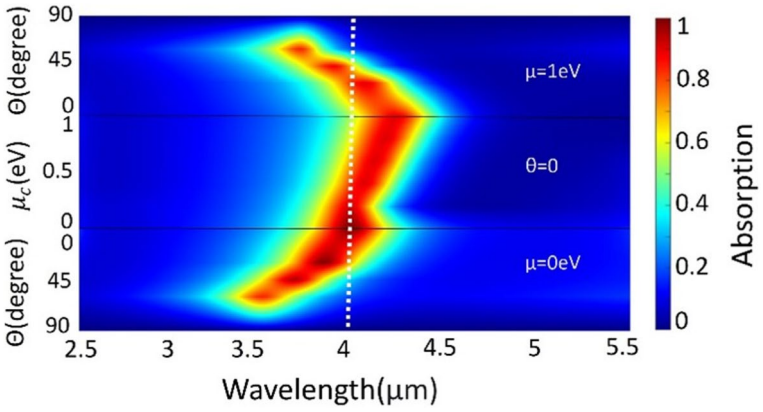

Fig. 8. The impact of altering the chemical potential and incident angle on the absorption spectrum of structure (e), optimized for an absorption peak at 4 μm. The absorption peak of this structure can be tuned from λ = 4 μm to λ = 4.22 μm by varying the chemical potential from 0 eV to 1 eV. Remarkably, there is substantial switchability, resulting in a decrease in absorption at 4 μm from 100–56% during the transition from 0 eV to 1 eV. The Structure still has more than 90% absorption by adjusting the angle up to 52°. changing in chemical potential and incident angle at the same time results in a deterioration of absorption performance.

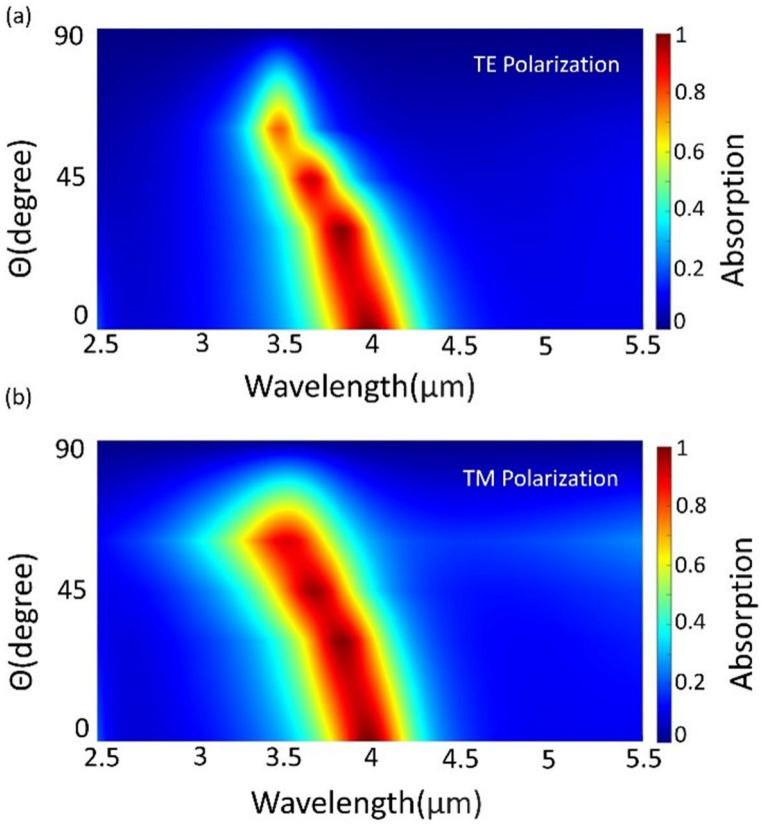

Fig. 9. The impact of varying the incident angle on the absorption spectrum for structure (e), optimized for absorption peak at 4 μm, for both (a) TE; and (b) TM polarizations. The structure exhibits superior absorption performance in TM polarization compared to TE polarization. Specifically, it functions as a PA with the flexibility to adjust the angle up to 60 degrees in TM polarization, while the limit is 47 degrees for TE polarizations.

To gain deeper insight into the absorption behavior and tunability of our structure, we analyzed the electric field distribution under different values of graphene chemical potential (μc). Figure 10 presents a combined visualization of simulation results from FDTD and COMSOL Multiphysics, highlighting the evolution of electric field intensity with μc. Figure 10(a) shows the normalized electric field intensity along the z-direction,

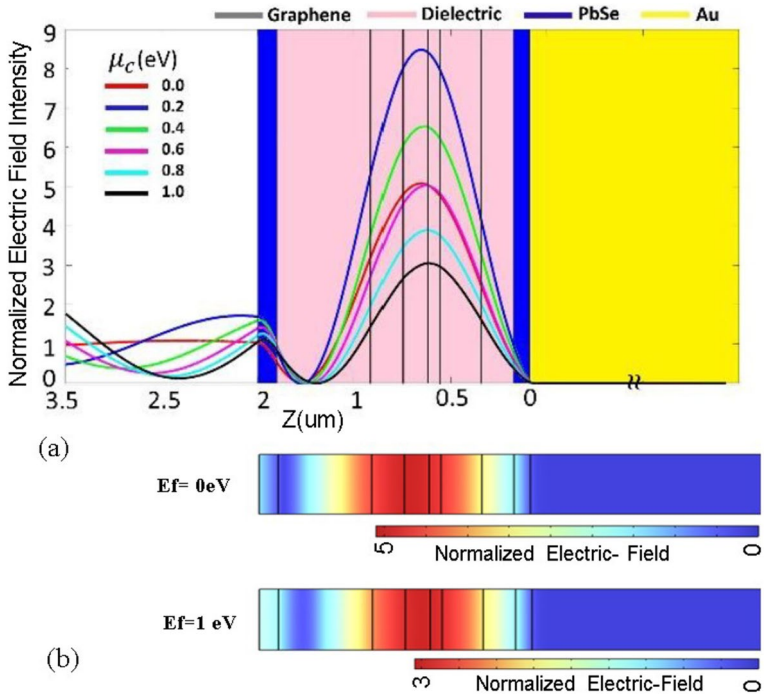

Fig. 10. (a): Simulated using the finite-difference time-domain (FDTD) method, this plot shows the normalized electric field intensity along the z-direction for multiple values of graphene chemical potential (μc = 0 to 1 eV). The simulation domain includes the air region above the structure, which allows visualization of both external and internal field behavior. At μc = 0.0 eV, where the structure is optimized for maximum absorption, the electric field in the air remains nearly constant, exhibiting an almost flat profile. This behavior indicates excellent impedance matching at the air-absorber interface, with negligible reflection—a hallmark of perfect absorption. As μc increases, the field confinement inside the multilayer weakens, confirming the switchable nature of the absorber.(b): Simulated using COMSOL Multiphysics, this panel shows the spatial distribution of the electric field inside the structure for two states: μc = 0 eV, with strong field localization, and μc = 1 eV, where the internal field intensity is significantly reduced. This independently confirms the tunable suppression of absorption and the modulation of plasmonic resonances in the multilayer stack.

including the air region, dielectric layers, graphene sheets, and gold substrate. This plot, simulated using FDTD, captures how the field is redistributed across the structure for μc ranging from 0 to 1 eV. At μc = 0 eV, where the structure is optimized for maximum absorption, we observe a flat and nearly constant electric field in the air region, indicating excellent impedance matching and minimal reflection. The strong field confinement inside the multilayer also suggests high absorptance. Interestingly, as μc increases, the electric field intensity inside the structure does not monotonically decrease. Instead, the peak field shifts in location and magnitude, reflecting changes in the internal mode structure and plasmonic response. However, this variation does not directly indicate improved absorption—rather, it reflects altered resonance conditions. Importantly, the non-flat air region field profiles at higher μc values indicate increased reflection and reduced absorption, consistent with the switching effect. To further validate these findings, Fig. 10(b) presents 2D electric field maps simulated using COMSOL Multiphysics for two representative chemical potentials: μc = 0 eV (top) and μc = 1 eV (bottom). At μc = 0 eV, the field is strongly confined within the multilayer, while at μc = 1 eV, the field penetration is significantly weaker—supporting the observation that electrical modulation of μc suppresses absorption. Together, these results show that perfect absorption is achieved through both impedance matching (zero reflection) and effective field localization, and that the structure's switching capability arises from the modulation of graphene's optical conductivity, which alters its ability to support resonant plasmonic modes.

In our optimized structure, it is also crucial to evaluate the sensitivity to fabrication errors and the tolerance range to ensure practical applicability. To address this, we analyze the impact of fabrication tolerances by varying the thickness of the thinnest layer by ± 5%. The original, optimized structure achieves 100% absorption at 3.991 μm, while the structures with + 5% and − 5% thickness variations exhibit 100% absorption at 4.002 μm and 3.988 μm, respectively. This demonstrates a wavelength shift of + 0.011 μm for a + 5% error and − 0.003 μm for a -5% error. The detailed graph of this analysis is provided in Supplemental Material S3.

Conclusion

This study introduces a novel graphene-based perfect absorber design operating in the mid-IR spectrum (3–5 μm), offering exceptional tunability, angular robustness, and switchability. Building on our previous work, this paper advances the concept of graphene-based aperiodic multilayer structures by proposing one single, narrowband PA design that achieves exceptional tunability and precision. Unlike traditional approaches that

Structure Type	Operation Wavelength	Absorption%	Thickness	Tunability and Switchability	Angle independent
Graphene Metasurface [30]	5–7 μm	>99%	~600 nm	>99% absorption at 6.9 μm to 95% at 6.5 μm by Changing gate voltage 0–10 V	Not reported
Nanopatterned Graphene [31]	8–12 μm	Up to ~90(Nanohole) Up to ~60 (Nanodisk)	~1.8 μm	~ 40% absorption at 9.46 μm to 60% at 8.33 μm(hole) 80% absorption at 9.07 μm to 90% at 8.73 μm(disk) by varying the chemical potential from -0.55 eV to -1 eV	Up to ~50°
Graphene Metamaterial [32]	9.12 μm	97.12%	~1.2 μm	97.12% absorption at 9.12 μm to 60% at 11.3 μm by Changing Chemical potential from 0.55 eV to 0.35 eV	Not reported
Graphene on Au-grating [37]	5–10 μm	90%	~70 nm	90% absorption at 6.28 μm to 90% at 6.22 μm by Changing gate voltage 0–1.6 V	Up to ~45° (absorption 85%)
Multilayer [21]	4.3–30 μm	>99%	~70 μm	Not tunable	Up to ~60°
Multilayer [22]	7.5–20 μm	>95%	~8 μm	Not tunable	Up to ~80° (wide-angle)
Multilayer with Ti Ring embedded [19]	3–5 μm	98.57%	~1.5 μm	Not Tunable	Up to ~60°
Multilayer [79]	3–5 μm	88.2%	~850 nm	Not Tunable	Angle-insensitive
Multilayer [80]	2-8.41	85%	~3.75 μm	Not Tunable	Up to 50° (TE), Up to 70° (TM)
Multilayer [11]	8–12 μm	>99.9% (dual), >80% (broadband)	~1.44 μm	Not Tunable	Up to 45° (dual), 30° (broadband)
Multilayer [This Work]	3–5 μm	>99.9%	~2 μm	>99.9% absorption at 4 μm to 95% absorption at 4.22 μm by changing chemical potential from 0 eV to 1 eV 100% absorption at 5 μm to 56% absorption by changing chemical potential from 0 eV to 1 eV	Up to 52°

Table 2. Comparison performance of recent graphene-based absorber in mid-IR with this work.

require distinct designs for each wavelength by altering material order or complex redesigns, our structure maintains a fixed material sequence while tuning only the layer thicknesses to control the absorption peak. This unique design enables systematic absorption peak shifts across the broad 3–5 μm wavelength range, with 0.25 μm resolution, without compromising performance. We also reduced the number of graphene layers to just five, significantly simplifying the design while maintaining near-perfect absorption efficiency. This hybrid approach precisely calibrates the absorption at specific mid-IR atmospheric windows, optimizing the structure for small size, weight, power, and cost. Moreover, the design exhibits high angular robustness, ensuring stable performance in real-world applications.

By leveraging aperiodic multilayer nanostructures optimized through advanced inverse design frameworks and hybrid micro-genetic algorithms, we achieved near-perfect absorption efficiencies of 99.99%. The dynamic tunability of the absorption peak was demonstrated by varying the chemical potential of graphene layers, enabling shifts of up to 0.22 μm without compromising performance. Similarly, the absorbers maintained robust performance under oblique light incidence, with absorption exceeding 90% at angles as high as 52° for some structures.

We further investigated the physical mechanisms underpinning these properties, highlighting the interplay of phase matching, surface plasmon excitation, and material refractive indices in determining the absorptive behavior. The redshift in absorption with increasing chemical potential and the blueshift with higher incident angles were explained through changes in resonance conditions and carrier density effects. Moreover, the proposed structure demonstrated significant tolerance to fabrication errors, retaining optimal absorption performance even with ± 5% variations in layer thickness.

These findings underscore the versatility and practical applicability of our graphene-based PA design for advanced mid-IR applications such as thermal photovoltaics, environmental monitoring, and infrared sensing[76–78]. The integration of tunability, compactness, and angular robustness establishes a scalable platform for the next generation of photonic and optoelectronic devices.

A comprehensive comparison of recent mid-IR absorbers—including multilayer, metasurface, and graphene-based designs—is presented in Table 2. This comparison highlights the advantages of our structure in achieving near-unity absorption across a wide wavelength range, with dynamic tunability, electrical switchability, and angular stability—all within a compact ~ 2 μm footprint. Unlike many existing approaches, our design avoids lithographic patterning or full structural redesign, offering a fabrication-friendly and scalable solution.

Data availability

The Supplementary Material provides comprehensive additional information supporting the manuscript's findings, including precise layer thicknesses for optimized structures (Tables S1 and S2) and fabrication tolerance analyses. Additionally, raw simulation data corresponding to the absorption spectra presented in the main figures, along with MATLAB scripts used to reproduce these figures, are publicly available at: https://github.com/INQUIRELAB/MidIR-Tunable-Switchable-Absorber/tree/main.

Received: 28 December 2024; Accepted: 24 April 2025
Published online: 21 May 2025

References

1. Monfared, Y. E. & Qasymeh, M. Graphene-assisted infrared plasmonic metamaterial absorber for gas detection. *Results Phys.* **23**, 103986 (2021).
2. Sharifi, S., Banadaki, Y. M., Nezhad, V., Veronis, G. & Dowling, J. Aperiodic multilayer graphene based tunable and switchable thermal emitter at mid-infrared frequencies. *J. Appl. Phys.*, **124**, 23 (2018).
3. Kazanskiy, N. L., Butt, M. A. & Khonina, S. N. Carbon dioxide gas sensor based on polyhexamethylene biguanide polymer deposited on silicon nano-cylinders metasurface. *Sensors* **21**(2), 378 (2021).
4. Seyyedmasoumian, S., Attariabad, A., Pourziad, A. & Bemani, M. Refractive index biosensor using metamaterial perfect absorber based on graphene in near-infrared for disease diagnosis. *IEEE Sens. J.* **22** (15), 14870–14877 (2022).
5. Yong, Z., Zhang, S., Gong, C. & He, S. Narrow band perfect absorber for maximum localized magnetic and electric field enhancement and sensing applications. *Sci. Rep.* **6**(1), 24063 (2016).
6. Yu, Z., Veronis, G., Fan, S. & Brongersma, M. L. Design of midinfrared photodetectors enhanced by surface plasmons on grating structures. *Appl. Phys. Lett.* **89**, 15 (2006).
7. McDowell, L. L., Mirzaei, M. R. & Shi, Z. Epitaxial CdSe/PbSeh heterojunction growth and MWIR photovoltaic detector. *Materials* **16**(5), 1866 (2023).
8. Xiao, J. et al. Improving light absorption and photoelectrochemical performance of thin-film photoelectrode with a reflective substrate. *RSC Adv.* **11** (27), 16600–16607 (2021).
9. Li, J. et al. Broadband solar energy absorber based on monolayer molybdenum disulfide using tungsten elliptical arrays. *Mater. Today Energy*. **16**, 100390 (2020).
10. Jain, P. et al. Ultra-thin metamaterial perfect absorbers for single-/dual-/multi-band microwave applications. *IET Microwaves Antennas Propag.* **14** (5), 390–396 (2020).
11. Wang, S., Wang, Y., Zhang, S. & Zheng, W. Mid-infrared broadband absorber of full semiconductor epi-layers. *Phys. Lett. A*. **381** (16), 1439–1444 (2017).
12. Luo, X. et al. Terahertz metamaterials broadband perfect absorber based on molybdenum disulfide. *IEEE Photonics Technol. Lett.* **34** (20), 1100–1103 (2022).
13. Thareja, V. et al. Electrically tunable coherent optical absorption in graphene with ion gel. *Nano Lett.* **15** (3), 1570–1576 (2015).
14. Huang, Z. T., Jiang, H. Y., Wang, Z. Y., Qing, Y. M. & Li, B. X. Thermally-electrically tunable graphene-based guided-mode resonant perfect absorber. *IEEE Photonics Technol. Lett.* **35** (4), 175–178 (2022).
15. Sreekanth, K. V. et al. A multiband perfect absorber based on hyperbolic metamaterials, *Scientific reports*, vol. 6, no. 1, p. 26272, (2016).
16. Hedayati, M. K., Faupel, F. & Elbahri, M. Tunable broadband plasmonic perfect absorber at visible frequency. *Appl. Phys. A*. **109**, 769–773 (2012).
17. Haas, J. & Mizaikoff, B. Advances in mid-infrared spectroscopy for chemical analysis. *Annual Rev. Anal. Chem.* **9**, 45–68 (2016).
18. Shiryaev, V. S. et al. Recent achievements in development of chalcogenide optical fibers for mid-IR sensing. *Fibers* **11**(6), 54 (2023).
19. Fang, Y., Gong, L., Huang, S., Yan, S. & Zhang, X. 3–5 Mm mid-infrared broadband perfect absorber based on Ti ring embedded structure. *IEEE Photon. J.* (2023).
20. Bossard, J. A. et al. Near-ideal optical metamaterial absorbers with super-octave bandwidth. *ACS Nano* **8**(2), 1517–1524 (2014). https://doi.org/10.1021/nn4057148.
21. Corrigan, T. D. et al. Broadband and mid-infrared absorber based on dielectric-thin metal film multilayers. *Appl. Opt.* **51** (8), 1109–1114 (2012).
22. Sahu, S. & Behera, G. Numerical study of mid-infrared broadband perfect absorber based on dielectric/aluminium doped zinc oxide multilayer films. *Opt. Mater.* **155**, 115776 (2024).
23. Chen, S. et al. Ultra-narrow band mid-infrared perfect absorber based on hybrid dielectric metasurface. *Nanomaterials* **9**(10), 1350 (2019).
24. Li, H., Wang, L. & Zhai, X. Tunable graphene-based mid-infrared plasmonic wide-angle narrowband perfect absorber. *Sci. Rep.* **6** (1), 36651 (2016).
25. Zhang, Y. et al. Independently tunable dual-band perfect absorber based on graphene at mid-infrared frequencies. *Sci. Rep.* **5** (1), 18463 (2015).
26. Yao, G. et al. Dynamically electrically tunable broadband absorber based on graphene analog of electromagnetically induced transparency. *IEEE Photonics J.* **8** (1), 1–8 (2015).
27. Wu, J. Broadband light absorption by tapered metal-dielectric multilayered grating structures. *Opt. Commun.* **365**, 93–98 (2016).
28. Khalilzadeh, H., Habibzadeh-Sharif, A. & Anvarhaghighi, N. Design of a broadband infrared absorber based on multiple layers of black phosphorus nanoribbons. *JOSA B*. **38** (12), 3920–3928 (2021).
29. Gupta, S. K. & Basu, P. K. Tunability in graphene based metamaterial absorber structures in mid-infrared region. *IEEE Photonics J.* **14** (3), 1–5 (2022).
30. Yao, Y. et al. Electrically tunable metasurface perfect absorbers for ultrathin mid-infrared optical modulators. *Nano Lett.* **14** (11), 6526–6532 (2014).
31. Safaei, A., Chandra, S., Leuenberger, M. N. & Chanda, D. Wide angle dynamically tunable enhanced infrared absorption on large-area nanopatterned graphene. *ACS Nano*. **13** (1), 421–428 (2018).
32. Sun, L. P., Zhai, X., Lin, Q., Liu, G. D. & Wang, L. L. Tunable nearly perfect absorber based on graphene metamaterials at the mid-infrared region. *Plasmonics* **13**, 1043–1048 (2018).
33. Wu, G. et al. Ultra-wideband tunable metamaterial perfect absorber based on vanadium dioxide. *Opt. Express*. **29** (2), 2703–2711 (2021).
34. Zhang, S. et al. Tunable narrowband shortwave-infrared absorber made of a nanodisk-based metasurface and a phase-change material ge 2 Sb 2 Te 5 layer. *Appl. Opt.* **59** (21), 6309–6314 (2020).
35. Raeis-Hosseini, N. & Rho, J. Metasurfaces based on phase-change material as a reconfigurable platform for multifunctional devices. *Materials* **10**(9), 1046 (2017).
36. Tripathi, A. et al. Tunable Mie-resonant dielectric metasurfaces based on VO2 phase-transition materials. *ACS Photonics*. **8** (4), 1206–1213 (2021).

37. Roy, S. & Debnath, K. Graphene-based electromechanically tunable subwavelength mid-IR perfect absorber. *Opt. Quant. Electron.* **55** (14), 1246 (2023).
38. Zong, S., Yao, Y., Liu, G., Liu, X. & Liu, Z. Actively tunable THz absorber for switchable operations between different absorption behaviors. *IEEE Photonics J.* **14** (6), 1–5 (2022).
39. Cao, T., Wei, C., Simpson, R. E., Zhang, L. & Cryan, M. J. Broadband polarization-independent perfect absorber using a phase-change metamaterial at visible frequencies. *Sci. Rep.* **4** (1), 3955 (2014).
40. Banadaki, Y., Dowling, J. & Sharifi, S. *Electrically Controllable and Tunable Electromagnetic-Field Absorber/Emitter Using Graphene/2D Material Multilayer Nanostructures*. Ed. (Google Patents, 2021).
41. Banadaki, Y. & Sharifi, S. *Graphene Nanostructures: Modeling, Simulation, and Applications in Electronics and Photonics* (Jenny Stanford Publishing, 2019).
42. Nazari, M., Banad, Y. M. & Sharif, S. S. Tunable nanophotonic multilayer structures to control mid-infrared atmospheric windows. In *2D Photonic Materials and Devices VII*. Vol. 12888 (SPIE, 2024).
43. Sharifi, S. Applications of stochastic optimization and machine learning in photonic nanostructures and quantum optical systems. *LSU Doctoral Dissertations* (2020).
44. Wu, C. J., Rau, Y. N. & Han, W. H. Enhancement of photonic band gap in a disordered quarter-wave dielectric photonic crystal. *Progress Electromagnet. Res.* **100**, 27–36 (2010).
45. Butt, M., Fomchenkov, S. & Khonina, S. Multilayer dielectric stack notch filter for 450–700 nm wavelength spectrum. In *CEUR Workshop Proceedings*. Vol. 1900. 1–4. (2017).
46. Novoselov, K. S. et al. Electric field effect in atomically thin carbon films. *Science* **306**(5696), 666–669 (2004).
47. Nair, R. R. et al. Fine structure constant defines visual transparency of graphene. *Science* **320**(5881), 1308–1308 (2008).
48. Vakil, A. & Engheta, N. Transformation optics using graphene. *Science* **332**(6035), 1291–1294 (2011).
49. Zhou, Q., Qiu, Q. & Huang, Z. Graphene-based Terahertz optoelectronics. *Opt. Laser Technol.* **157**, 108558 (2023).
50. Wirth-Lima, A., Silva, M. & Sombra, A. Comparisons of electrical and optical properties between graphene and silicene—A review. *Chin. Phys. B.* **27** (2), 023201 (2018).
51. Chen, P. Y. & Alu, A. Atomically thin surface cloak using graphene monolayers. *ACS Nano*. **5** (7), 5855–5863 (2011).
52. Chen, P. Y., Huang, H., Akinwande, D. & Alu, A. Graphene-based plasmonic platform for reconfigurable Terahertz nanodevices. *Acs Photonics*. **1** (8), 647–654 (2014).
53. Falkovsky, L. & Pershoguba, S. Optical far-infrared properties of a graphene monolayer and multilayer. *Phys. Rev. B*. **76** (15), 153410 (2007).
54. Furchi, M. et al. Microcavity-integrated graphene photodetector. *Nano Lett.* **12** (6), 2773–2777 (2012).
55. Stauber, T., Noriega-Pérez, D. & Schliemann, J. Universal absorption of two-dimensional systems. *Phys. Rev. B*. **91** (11), 115407 (2015).
56. Stauber, T., Peres, N. M. & Geim, A. K. Optical conductivity of graphene in the visible region of the spectrum. *Phys. Rev. B*. **78** (8), 085432 (2008).
57. Kumar, V. Linear and nonlinear optical properties of graphene: a review. *J. Electron. Mater.* **50** (7), 3773–3799 (2021).
58. Jablan, M., Buljan, H. & Soljačić, M. Plasmonics in graphene at infrared frequencies. *Phys. Rev. B*. **80** (24), 245435 (2009).
59. Grigorenko, A. N., Polini, M. & Novoselov, K. Graphene plasmonics. *Nat. Photonics*. **6** (11), 749–758 (2012).
60. Alisultanov, Z. The thermodynamics of electrons and the thermoelectric transport in epitaxial graphene on the size-quantized films. *Phys. E: Low-dimensional Syst. Nanostruct.* **69**, 89–95 (2015).
61. Romasanta, L. J., Hernández, M., López-Manchado, M. A. & Verdejo, R. Functionalised graphene sheets as effective high dielectric constant fillers. *Nanoscale Res. Lett.* **6**, 1–6 (2011).
62. Prajzler, V., Chlupatý, V. & Šaršounová, Z. The effect of gamma-ray irradiation on bulk optical plastic materials. *J. Mater. Sci.: Mater. Electron.* **31**, 22599–22615 (2020).
63. Slonov, A. et al. Investigation of the properties of polyphenylene sulfone blends. *Materials* **15**(18), 6381 (2022).
64. El-Hibri, M. J. & Shari, W. A. Polyarylethersulfones. In *Handbook of Thermoplastics*. (CRC, 2015).
65. Rastkar Mirzaei, M. & Shi, Z. Room-temperature nanostructured PbSe/CdSe mid-infrared photodetector: Annealing effects. *J. Vac. Sci. Technol. B* **42**, 1 (2024).
66. Wei, S. H. & Zunger, A. Electronic and structural anomalies in lead chalcogenides. *Phys. Rev. B*. **55** (20), 13605 (1997).
67. Dortaj, H. et al. High-speed and high-precision PbSe/PbI2 solution process mid-infrared camera. *Sci. Rep.* **11** (1), 1533 (2021).
68. Suzuki, N., Sawai, K. & Adachi, S. Optical properties of PbSe. *J. Appl. Phys.* **77** (3), 1249–1255 (1995).
69. Zhao, Y. et al. Dual band and tunable perfect absorber based on dual gratings-coupled graphene-dielectric multilayer structures. *Opt. Express*. **27** (4), 5217–5229 (2019).
70. Bartek, M., Correia, J. H. & Wolffenbuttel, R. F. Silver-based reflective coatings for micromachined optical filters. *J. Micromech. Microeng.* **9** (2), 162 (1999).
71. Cornelius, C. M. & Dowling, J. P. Modification of planck blackbody radiation by photonic band-gap structures. *Phys. Rev. A*. **59** (6), 4736 (1999).
72. Granier, C. H. et al. Optimized aperiodic multilayer structures for use as narrow-angular absorbers. *J. Appl. Phys.* **116**, 24 (2014).
73. Tremblay, G., Gillet, J. N., Sheng, Y., Bernier, M. & Paul-Hus, G. Optimizing fiber Bragg gratings using a genetic algorithm with fabrication-constraint encoding. *J. Lightwave Technol.* **23** (12), 4382 (2005).
74. Jiang, X. et al. Metasurface based on inverse design for maximizing solar spectral absorption. *Adv. Opt. Mater.* **9** (19), 2100575 (2021).
75. Katoch, S., Chauhan, S. S. & Kumar, V. A review on genetic algorithm: past, present, and future. *Multimedia Tools Appl.* **80**, 8091–8126 (2021).
76. Sharif, S. Evolutionary-based inverse design of 2D materials multilayer structures for next-generation IR smart sensing. In *Quantum Sensing and Nano Electronics and Photonics XXI*. Vol. 13376 (SPIE, 2025).
77. Nazari, M., Banad, Y. M. & Sharif, S. S. Advancing Mid-Infrared Sensing: A Novel Approach to Design Focal Plane Arrays for Enhanced Detection. In *Frontiers in Optics*. (Optica Publishing Group, 2023).
78. Sharif, S. S. & Banad, Y. M. Revolutionizing Infrared Detection in Defense Applications: A Nanophotonic Approach Leveraging 2D Materials for Enhanced Mid-IR Absorption. In *2024 IEEE Research and Applications of Photonics in Defense Conference (RAPID)*. (IEEE, 2024).
79. Cui, Q., Wu, Y., Wang, Y. X., Han, C. Q. & Yan, C. C. Multilayer thin film mid-infrared broadband absorber with high visible light transmittance. *Opt. Mater.* **157**, 116091 (2024).
80. Zhang, H. et al. Ultra-broadband mid-infrared absorption based on photonic topological transition and anti-reflection effect. *Opt. Laser Technol.* **185**, 112607 (2025).

Acknowledgments

This research is based upon work supported by the Air Force Office of Scientific Research under award number FA9550-25-1-0117.The financial support was provided by the University of Oklahoma Libraries' Open Access Fund.

Author contributions

M. Nazari conducted all simulations and prepared the first draft of the manuscript. The main idea and the computational codes were developed by S. Sharif, who also extensively edited and finalized the manuscript for submission to Scientific Reports. Y. Banad contributed significantly to idea generation, provided critical feedback, and made substantial contributions to manuscript revision and refinement through his valuable comments. All authors reviewed and approved the final manuscript.

Declarations

Competing interests

The authors declare no competing interests.

Additional information

Supplementary Information The online version contains supplementary material available at https://doi.org/10.1038/s41598-025-99995-6.

Correspondence and requests for materials should be addressed to S.S.

Reprints and permissions information is available at www.nature.com/reprints.

Publisher's note Springer Nature remains neutral with regard to jurisdictional claims in published maps and institutional affiliations.